TOPEX/Poseidon Microwave Radiometer (TMR): III. Wet Troposphere Range Correction Algorithm and Pre-Launch Error Budget

Stephen J. Keihm, Michael A. Janssen, and Christopher S. Ruf

Abstract—**The sole mission function of the TOPEX/Poseidon Microwave Radiometer (TMR) is to provide corrections for the altimeter range errors induced by the highly variable atmospheric water vapor content. The three TMR frequencies are shown to be near-optimum for measuring the vapor-induced path delay within an environment of variable cloud cover and variable sea surface flux background. After a review of the underlying physics relevant to the prediction of 5–40 GHz nadir-viewing microwave brightness temperatures, we describe the development of the statistical, two-step algorithm used for the TMR retrieval of path delay. Test simulations are presented which demonstrate the uniformity of algorithm performance over a range of cloud liquid and sea surface wind speed conditions. The results indicate that the inherent algorithm error (assuming noise free measurements and an exact physical model) is less than 0.4 cm of retrieved path delay for a global representation of atmospheric conditions. An algorithm error budget is developed which predicts an overall algorithm accuracy of 0.9 cm when modeling uncertainties are included. When combined with expected TMR antenna and brightness temperature accuracies, an overall measurement accuracy of 1.2 cm for the wet troposphere range correction is predicted.**

I. Introduction

SATELLITE microwave radiometers have been successfully used to monitor the temporal and spatial variations of sea surface and atmospheric properties on a global scale since the launch of the Soviet Cosmos-243 instrument in 1969. The retrieved properties have included temperature profiles [1]–[3], soil moisture [4], [5], sea ice [6]–[8], snow cover [9], [10], and, over the open oceans, rain rate [11]–[13], atmospheric vapor [14]–[16] and cloud liquid [17], [18], sea surface temperature [19], [20], and wind speed [21]–[23]. Grody [24] provides a complete review of past, present, and planned future satellite microwave instruments, including their operational characteristics and applications.

One of the satellite-retrieved properties, the atmospheric water vapor burden, is a major source of uncertainty in ranging measurements through the earth's atmosphere due to its effect on the index of refraction. Signal propagation delay due to water vapor is highly variable with time and location, producing range measurement errors of ~3–45 cm if uncorrected. For satellite radar altimeter measurements of sea surface topography, the instrument-related ranging errors are now down to the 2–4 cm level [25]. Thus, precise estimates of the vapor-induced range corrections are clearly required to fully utilize the current altimeter technology.

The first satellite sea-level altimeter measurements were obtained from the Seasat satellite, launched in 1978. The satellite also included the Scanning Multichannel Microwave Radiometer (SMMR). The SMMR was designed to map a variety of sea surface and atmospheric properties, including vapor burden, with almost complete global coverage on a 24 hour time scale [26]. It operated in a conical scan mode with constant 42° displacement from the nadir direction. Its use for providing a time co-located range correction for the nadir viewing altimeter was limited by the large spatial decorrelations of water vapor over 500 km distances.

An alternative method for providing temporally and spatially co-located range corrections for satellite altimetry measurements is the use of climatological models constrained by real time measurements of the critical atmospheric parameters from a global network of radiosondes and weather stations. The GEOSAT altimetry mission, which does not include a companion radiometer, has used the PERIDOT climatological model of the French Meteorologie Nationale to provide range corrections with estimated accuracy of 10% [27]. The major drawback to the use of the climatological models for satellite altimetry range corrections is that the network interpolation errors can be large for anomalous conditions such as regions of weather fronts and high convective activity.

Advances in altimeter instrumentation have stimulated satellite missions which include single purpose microwave radiometers designed specifically to provide the altimeter range correction due to water vapor. The radiometers are nadir viewing and co-aligned with the altimeters. The European ERS-1 satellite, an altimetry mission launched in 1987, includes a radiometer operating at 23.8 and 36.5 GHz which is designed to provide vapor-related range corrections with 2 cm accuracy [28]. The TOPEX/Poseidon altimetry satellite, launched in August of 1992, includes a three-channel (18, 21, and 37 GHz) nadir viewing radiometer (TMR), designed to provide range corrections due to vapor with 1.2 cm accuracy [25]. Plans for GEOSAT, ERS-1, and TOPEX follow-on altimeter missions also include nadir viewing radiometers for the primary purpose

Manuscript received September 7, 1993.

S. J. Keihm is with the Ball Corporation, under contract to the Jet Propulsion Laboratory, California Institute of Technology, Pasadena, CA 91109-8099 USA.

M. A. Janssen is with the Jet Propulsion Laboratory, California Institute of Technology, Pasadena, CA 91109 USA.

C. S. Ruf is with the Department of Electrical Engineering, The Pennsylvania State University, University Park, PA 16802 USA.

IEEE Log Number 9406435.

of providing corrections to the altimeter range measurements. In addition to vapor related retrievals, these radiometers will also provide valuable data related to cloud liquid abundance and, possibly, sea surface wind speed.

The remainder of this paper addresses the development of the algorithm for the retrieval of vapor related range corrections from the TMR brightness temperature measurements. Algorithms related to the TMR antenna temperature calibration [29] and antenna pattern correction [30] are discussed in companion papers within this volume. Because instruments similar to TMR will be used to support future altimetry missions, the physical basis for interpreting 5–40 GHz nadir, ocean-viewing satellite radiometer measurements will be presented in Section II. This section will begin with the fundamental concepts relating water vapor abundance to signal propagation delays, then describe the basis for relating water vapor and other atmospheric and sea surface properties to the satellite microwave measurements. Section II concludes with an analysis of the relative sensitivities of the 18, 21, and 37 GHz TMR channels to relevant atmospheric and sea surface properties.

Section III begins with a brief discussion of the general methodologies employed for atmospheric and sea surface property retrievals using satellite microwave radiometers. The algorithm developed for retrieval of the TOPEX wet troposphere range correction is then presented, along with simulation test results. Section III also includes an analysis of two-frequency retrievals which is relevant to cost versus performance issues for future altimetry missions. In Section IV the algorithm and overall range correction error analysis is presented in conjunction with the plans for post-launch verification. This analysis evaluates the total error for the TMR wet troposphere correction and incorporates the radiometer calibration and antenna pattern corrections discussed in the companion papers [29], [30].

II. Background Physics

A. Vapor-Induced Path Delay

The effects of all atmospheric gases on the propagation of a signal through the atmosphere, expressed as a range correction, or zenith path delay, is the difference between electrical and geometrical path length for the range signal

$$\mathrm{PD} = \int_0^s n(z)dz - S = \int_0^s (n-1)dz = 10^{-6}\int_0^s N(z)dz \tag{1}$$

where

$n =$ the refractive index along the ranging signal path,
$S =$ the atmospheric height above which propagation effect are insignificant, and
$N =$ the refractivity, defined to be the difference between the index of refraction in the atmosphere and in vacuum, in parts per million.

The refractivity may be expressed as the sum of "dry" (hydrostatic) and "wet" (vapor-induced) components [31] in which the dry component depends only on surface pressure and the wet component is proportional to vapor density divided by physical temperature. Based on the measurements of [32], the wet refractivity component due to vapor is

$$N_v = 1763\rho_v/T \tag{2}$$

yielding a vapor induced path delay component given by

$$\mathrm{PD}_V = 1.763^{*}10^{-3}\int_0^s (\rho_V/T)dz \tag{3}$$

where ρ_v = vapor density in g/m^3, T = physical temperature in Kelvins, and z is in meters. Extensive evaluation [33] of the experimental and theoretical determinations of the vapor induced refractivity component indicate that the relationship expressed in (3) is accurate to the 0.5% level. At microwave frequencies <30 GHz, the refractivity component induced by the weak 22 GHz vapor resonance feature is practically nondispersive and the path delay expressed in (3) can be considered frequency-independent.

The wet path delay also includes a small component due to cloud liquid when present. To sufficient accuracy, the liquid contribution can be represented by [34]

$$\mathrm{PD}_L = 1.6L_z \tag{4}$$

where L_z is the integrated liquid in mm. Typically, for non-raining conditions, $L_z < 1.5$ mm so that PD_L rarely exceeds 1% of PD_V. Hereafter, unless otherwise noted, the term path delay (PD) will refer to the vapor induced component (3).

Since ~95% of the atmospheric water vapor resides in the lower troposphere (z <5 km), where average temperatures are typically in the 270–290°K range, the path delay is primarily correlated with vapor burden, $V_z = \int_0^s \rho_v dz$, and is highly variable with time and location. The correlation is shown in Fig. 1, based on integrations of radiosonde data from low, moderate, and high humidity sites. The upturn at low vapor conditions is indicative of the magnitude of the temperature effect in (3). Dry conditions are correlated with low tropospheric temperatures while the highest vapor conditions require high temperatures to hold the large amounts of water. It is clear from Fig. 1 that with a vapor-dependent

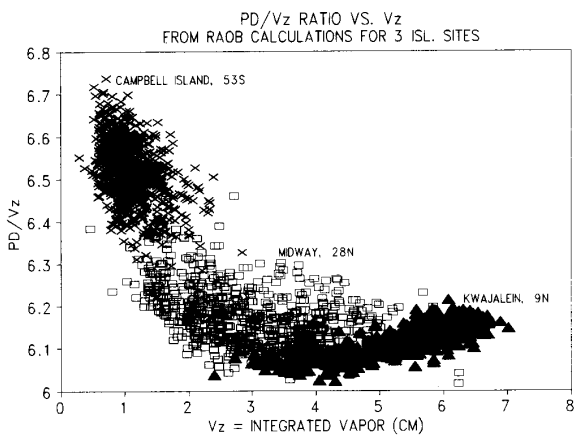

Fig. 1. Variation of the ratio of vapor-induced path delay to vapor burden with vapor burden from radiosonde calculations.

correction, path delay can be accurately determined from satellite measurements which are sensitive to the atmospheric vapor burden. The satellite brightness temperatures correlate with path delay through the absorption/emission properties of water vapor, as revealed in the equation of radiative transfer.

B. Radiative Transfer Equation

For a nonscattering (no rain) atmosphere the microwave flux measured by a satellite-borne radiometer can be expressed as a brightness temperature which is considered to be the sum of three frequency (ν) dependent components [24]

$$T_b(\nu) = T_u(\nu) + T_e(\nu)e^{-\tau(\nu)} + T_r(\nu)e^{-\tau(\nu)} \quad (5)$$

where $\tau(\nu)$ is the opacity from the earth's surface to the satellite altitude, H,

$$\tau(\nu) = \int_0^H \alpha(z)dz \quad (6)$$

and $\alpha(z)$ is the frequency dependent atmospheric absorption in nepers/km.

$T_u(\nu)$ is the contribution from the upwelling radiation of the atmosphere, integrated from the surface at $z = 0$ to the satellite height at $z = H$

$$T_u(\nu) = \int_0^H T(z)\alpha(z)e^{-\int_z^H \alpha(z')dz'}dz \quad (7)$$

where $T(z)$ is the atmospheric temperature in Kelvins.

Equation (7) simply states that the atmosphere's upwelling contribution is the sum of the upward emissions at each height $[T(z)\alpha(z)]$, attenuated by the absorption of the intervening atmosphere $[e^{-\int_z^H \alpha(z')dz'}]$.

$T_e(\nu)$ is the flux emitted by the surface and can be simply expressed as the product of an effective emissivity, $\epsilon(\nu)$,and the surface temperature, T_s:

$$T_e(\nu) = \varepsilon(\nu)T_s. \quad (8)$$

The effective emissivity is actually a complicated function of the bistatic scattering coefficients of the surface and the variation of downwelling flux with incident angle, and will be discussed further in Section II-D.

$T_r(\nu)$ is the contribution from the downwelling atmosphere and cosmic background flux, T_c, which is reflected at the surface into the zenith direction:

$$T_r(\nu) = \left[\int_0^H T(z)\alpha(z)e^{-\int_0^z \alpha(z')dz'}dz + T_c(\nu)e^{-\tau(\nu)}\right] \times [1 - \varepsilon(\nu)] \quad (9)$$

where $[1-\varepsilon(\nu)]$ equals the surface reflectivity from Kirchoff's law. The integral term is the downwelling atmospheric flux at the surface, analogous to (7) for the upwelling component. Note in (9) that the attenuation of the cosmic background flux assumes that the satellite height is above the level of significant atmospheric absorption. The cosmic background contribution, T_c, is frequency dependent to account for departures from the Rayleigh-Jeans approximation [35].

The satellite-measured microwave brightness temperature, as expressed through (5)–(9), is seen to depend on four variable properties: the atmospheric temperature and absorption profiles, and the surface temperature and emissivity. The absorption profiles, in turn, depend on the highly frequency dependent properties of three atmospheric components: oxygen, water vapor, and liquid water suspended in clouds. The oxygen is well mixed, with absorption properties completely determined by the pressure, $P(z)$, and temperature profiles. The vapor and liquid abundances are highly variable, with absorption properties dependent on temperature, pressure (vapor only), and component densities $[\rho_v(z), \rho_L(z)]$. Thus, in general, the satellite microwave measurements depend on two surface and four atmospheric profile properties: $T_s, \varepsilon(\nu), T(z), P(z), \rho_v(z)$, and $\rho_L(z)$.

The capability for retrieving any of these properties from satellite measurements is determined by the atmospheric absorption spectra. For example, at frequencies near the 60 GHz oxygen absorption peak, the opacity is sufficiently high ($\tau \gg 1$) that the surface flux and emissions from the lower troposphere are not "seen" by a satellite radiometer, and the measurements are primarily diagnostic of the temperature profile in the stratosphere and upper troposphere. At frequencies from 5–40 GHz, the opacity is sufficiently small ($0.01< \tau <1.0$) that contributions from both the surface and atmosphere are significant, with the atmospheric component heavily weighted toward the lower troposphere where the bulk of the water vapor and all of the liquid water reside. At frequencies below 5 GHz, the atmosphere is essentially transparent ($\tau < 0.01$) so that radiometer measurements are primarily diagnostic of surface properties.

In the remainder of this section, the diagnostic capabilities of open ocean satellite measurements in the frequency range 5–40 GHz will be assessed, with the ultimate purpose of demonstrating that the TMR frequencies are near optimum for estimating water vapor abundance in the presence of variable cloud liquid and surface winds. The approach will be to begin with a description of the atmospheric absorption and sea surface emissivity properties, including model selection and uncertainties. The relative contributions of the surface flux and atmospheric oxygen, vapor, and liquid emissions to satellite brightness temperature spectra will then be compared. Finally, sensitivity spectra will be developed which illustrate the relative response of the satellite measurements to representative variations of the atmospheric and sea surface properties.

C. Atmospheric Absorption Models

The following models have been adopted for the atmospheric absorption properties of oxygen, water vapor, and suspended cloud liquid.

For oxygen, a modified version of the most recent model of Liebe, Rosenkranz and Hufford (LRH) [36] is used for the 5–40 GHz range. The LRH model is based on extensive laboratory measurements of the absorption parameters for the cluster of overlapping, pressure broadened lines between 50 and 70 GHz. The effects of the oxygen absorption features

at 118 GHz and higher frequencies are also included in the model. The LRH model reproduces the laboratory absorption measurements with accuracies better than 2% for lower troposphere conditions over the 50–70 GHz spectral range. At higher altitudes, where the lines are resolved, the absolute model accuracies are at the 0.01 neper/km level. For frequencies less than 40 GHz, the oxygen wing absorption falls below the 0.01 neper/km level, and the fractional accuracy has been difficult to determine. Based on recent 31 GHz brightness temperature comparisons between ground-based radiometer measurements and calculations from radiosonde data [37], the LRH model predictions appear to be ~7% low at 31 GHz. This result is consistent with other, more extensive radiometer–radiosonde comparisons [38] and high altitude (3.8 km) radiometric measurements at 33 GHz [39]. Based on these results, we have adopted an oxygen absorption model equivalent to 1.07 × LRH for the 5–40 GHz region. The 7% adjustment at the low levels of the <40 GHz absorption is not unreasonable, considering the uncertainties of the far wing absorption for oxygen lines (Rosenkranz, personal communication). Based on the comparison data, we estimate an uncertainty of 5% for the adopted 5–40 GHz oxygen absorption model.

For vapor, we use the 1987 model of Liebe and Layton (40), with a +8% adjustment, also based on the radiometer–radiosonde comparisons [37], [38]. The model uses the Van Vleck–Weiskopf line shape [41] to compute the pressure broadened 22.2 GHz water vapor resonance absorption, with wing contributions from higher frequency absorption lines and an empirical "continuum" added. The continuum term accounts for discrepancies between measured and modeled vapor absorption in window regions of the microwave spectrum [42]. The +8% adjustment is based mainly on 22.2 GHz radiometer–radiosonde comparisons [37] and is also consistent with the only available laboratory measurements of the 22.2 GHz absorption feature [43]. Based on the accuracies of radiosonde humidity measurements and the consistency of the model with independent radiometer–radiosonde comparisons, we estimate a 4% uncertainty for the adopted vapor absorption model.

For suspended cloud liquid droplets of radii <100 microns, the Rayleigh approximation can be used to calculate the 5–40 GHz absorption to an accuracy of several percent [24]. The absorption is proportional to the cloud liquid density and depends on the temperature-varying properties of the dielectric constant of water. For the TMR algorithm modeling, we have adopted the liquid absorption model of [40]. Comparisons with other liquid droplet absorption models reveal differences at the 5% level or less.

D. Sea Surface Emissivity

The reflected brightness temperature component (9) will, in general, include contributions from a distribution of downwelling angles, weighted by the bistatic scattering coefficients of the surface [45]. For the sea surface, roughness at all scales must be considered, as well as emissivity variations due to the presence of foam. Both the roughness and fractional foam coverage are strongly correlated with the wind shear at the sea surface-atmosphere interface. Because friction velocities are difficult to measure directly, wind-induced effects on the sea surface flux are normally correlated with the wind speed at a 20 m reference height [46].

For roughness due to large-scale waves, the scattering coefficients can be computed by modeling the sea surface as a Gaussian distribution of tilted facets, each scattering into the view angle according to Fresnel reflection. Using the Cox and Munk [47] sun glitter experimental data relating the alongwind and crosswind sea surface rms slopes to wind speed, [48] showed that brightness temperature enhancements of tens of degrees (horizontal polarization) and ~−3 to 3°K (vertical polarization) will occur for view angles in the 30–70° range and wind speeds up to 14 m/s. At nadir, however, the large scale roughness effects are small, ~1°K or less. This result is due to the slow variation of both the downwelling sky brightness and the Fresnel reflectivity with view angle variations from nadir. The inherent averaging of horizontally and vertically polarized reflected components, which vary with view angle almost equally but with opposite sign near nadir, also contributes to the null effect.

For small scale roughness, diffraction of the downwelling flux by surface capillary waves produces emissivity variations which depend primarily on the rms height of the small-scale waves [49]. For nadir observations, the principal effect appears to be a polarization anisotropy related to wind direction. A number of Soviet experiments [50]–[52] have clearly demonstrated this effect by comparing aircraft measurements made with the observing polarization vector alternately parallel to the alongwind and crosswind directions. The data indicates an upwind-minus-crosswind enhancement of ~2–4°K for wind speeds >10 m/s and observing frequencies from 15–40 GHz. The anisotropy decreases rapidly for frequencies below 10 GHz and wind speeds below 10 m/s. Some of the data does suggest a slight increase in the anisotropy as the frequency varies from 15 to 37 GHz. The Soviet data, however, does not reveal the absolute brightness temperature enhancement (relative to a calm sea) for either the alongwind or crosswind observations.

In terms of absolute nadir enhancements, other aircraft measurements [53], [54] have not detected sea surface microwave flux increases for wind speeds less than ~7 m/s. Above the 7 m/s threshold, the nadir measurements show a consistent 0.8–1.2°K increase per m/s of wind speed for frequencies in the range 10–37 GHz. Below frequencies of ~7.5 GHz, the wind speed enhancements fall off rapidly, with measured effects a factor of 10 less at 1.4 GHz [54].

The nadir wind speed flux enhancements are not predicted by the large scale roughness models. Rather, they are due to the onset of foam (streaks and white caps) which has been observed to occur at wind speeds of ~7 m/s [53]. The frequency dependence of the foam signature can be explained by the effective foam thickness and its effect on the underlying water surface [54]. A model proposed in [46], in which the effective foam coverage is assumed to be frequency dependent, and the effective foam emissivity =1.0, matches the experimental data.

Based on the above results, we have adopted a two-component formulation for the effective nadir emissivity of the sea surface. The first component is the specular contribution which depends only on the dielectric properties of the sea surface, which, in turn, depend on temperature, salinity, and frequency. The dependencies formulated in [55], based on laboratory measurements at 1.43 and 2.65 GHz, and a reevaluation of earlier, higher frequency laboratory data, are used here. The open ocean salinity is assumed constant at 35 parts per thousand. Klein and Swift estimated the resultant modeling uncertainty to be less than 0.1% in terms of sea surface specular emissivity and brightness temperature for frequencies below 8.5 GHz. The accuracy at higher frequencies is in question due to uncertainties in extrapolation of the laboratory measurements of the dielectric properties.

More recently, [56] reviewed the available laboratory data and noted that significant discrepancies exist in the derived dielectric constant properties above 10 GHz. He rederived dielectric property expressions and presented a new temperature dependent formulation for the spectral emissivity at a view angle of 51° and frequencies of 19, 22, and 37 GHz. A comparison with emissivity calculations using the Klein–Swift expressions reveal the resultant sea surface brightness temperature differences to be T_s dependent, but less than 1°K at 19 and 22 GHz. At 37 GHz, the Klein–Swift model yields ~2°K higher sea surface fluxes than the Wentz model for T_s =275°K. At 295°K, the 37 GHz differences are negligible. It thus appears that the uncertainty in the sea surface specular flux model increases with frequency above 10 GHz to a level of ~2°K at 37 GHz, and that the errors will vary with sea surface temperature.

Results of the Klein–Swift model calculations for the specular components of sea surface nadir emissivity and flux are shown in Fig. 2. It is noteworthy that, due to the inverse dependence of emissivity on T_s, the specular sea surface flux is nearly independent of surface temperature at the TMR frequencies of 18 and 21 GHz.

The second component of our sea surface nadir emissivity model is due to wind speed variations and uses the [46] model for the effective fractional coverage of black body foam:

$$\begin{aligned} f_s &= 0 \text{ for } W < 7 \text{ m/s} \\ &= 0.006(1 - e^{-\nu/7.5})(W - 7) \quad \text{for } W > 7 \text{ m/s} \end{aligned} \tag{10}$$

where f_s is the fractional foam coverage and W is the wind speed 20 m above the surface. For W <7 m/s, a small wind speed effect due to the small scale roughness [57] is included which produces ~1°K of frequency-independent T_b enhancement at W =7 m/s (relative to the specular case). The total nadir emissivity is then expressed as

$$\begin{aligned} \varepsilon_{\text{tot}} &= \varepsilon_{\text{spec}} + 0.0005^* W \text{ for } W < 7 \text{ m/s} \\ &= (\varepsilon_{\text{spec}} + 0.0035)(1 - f_s) + f_s \text{ for } W > 7 \text{ m/s}. \end{aligned} \tag{11}$$

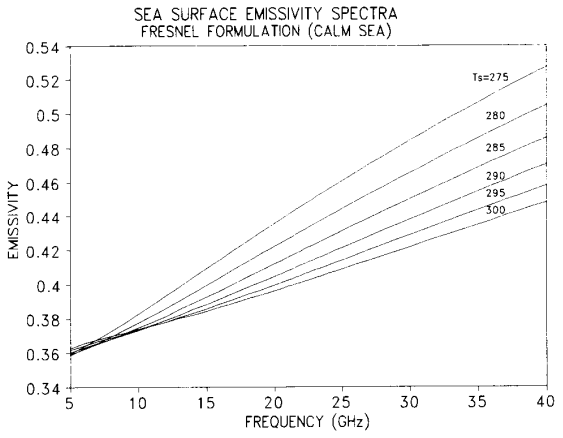

(a)

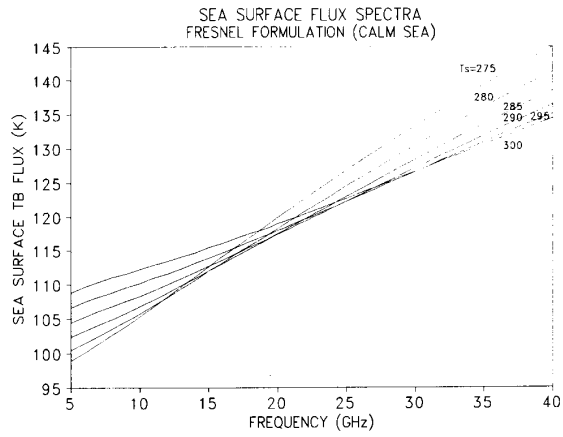

(b)

Fig. 2. (a) Sea surface specular emissivity spectra from 5–40 GHz based on the dielectric properties model of [55]. (b) Sea surface specular flux component spectra from 5–40 GHz based on the dielectric properties model of [55].

E. Satellite Brightness Temperature Components and Sensitivity Spectra

Based on the above formulations for atmospheric absorption and sea surface emission properties, we now illustrate the relative contributions of the sea surface and atmospheric components to nadir-viewing satellite microwave measurements. Fig. 3 shows the buildup of these components from the case of no atmosphere (sea surface flux only) to the addition of oxygen, then vapor, then cloud liquid. The calculations assumed calm seas (W <7 m/s), T_s =295°K, and nominal mid-latitude, open-ocean atmospheric conditions. At the surface T =300°K, P =1013 mb, and ρ_v =15 g/m^3. The temperature decreases with altitude with a lapse rate of 7°K/km to the tropopause at 11.4 km, then holds constant at 220°K to the top of the atmosphere. The pressure varies hydrostatically. The water vapor decreases exponentially with a scale height of 2 km. The resultant value for integrated vapor, V_z =3 cm, is near the mean of the expected range of global values.

The specular sea surface background flux is clearly the dominant component for nadir measurements over the 5–40 GHz

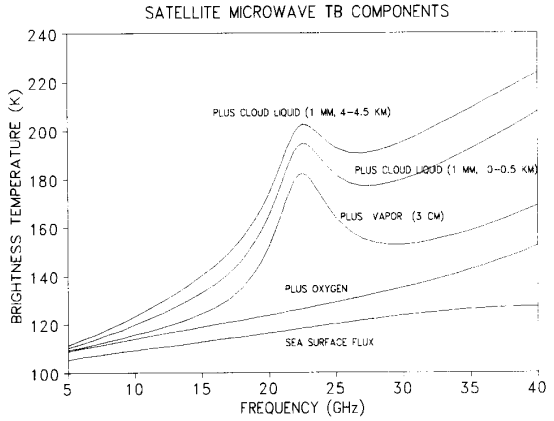

Fig. 3. Spectra of satellite microwave brightness temperature components from 5–40 GHz.

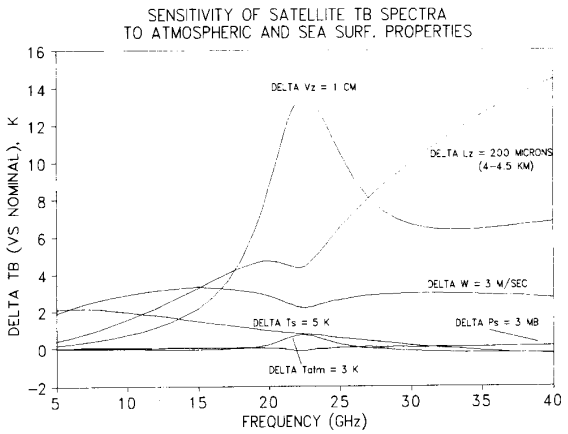

Fig. 4. Sensitivity spectra of satellite brightness temperatures from 5–40 GHz. Individual curves show the brightness temperature changes relative to the nominal model atmosphere due to increments in atmospheric and sea surface parameters that represent 10–20% of their total expected variability.

frequency range. When the atmosphere is included, the sea surface flux component shown will be reduced by ~1–20% due to the frequency dependent opacity. With the addition of a dry atmosphere (oxygen curve), 3–25°K is added to the satellite spectra over 5–40 GHz. This includes the reflected, as well as direct, sky radiation. The oxygen component changes by less than 1% per degree Kelvin of atmospheric temperature variation. Thus, variations over open-ocean climates are small.

When the nominal model vapor burden (V_z =3 cm) is added, the satellite brightness temperature spectrum peaks near the 22.2 GHz water vapor line, with almost no contribution below 10 GHz. Variability in the total vapor abundance will amplify the nominal model spectrum by a factor ranging from ~0.1–2.0. The addition of a heavy (L_z =1 mm) nonraining cloud layer constitutes a $\sim\nu^2$ component which is strongly dependent on cloud height (temperature). The examples shown are for cloud layers from 0–0.5 km (average temperature = 298°K) and 4.0–4.5 km (average temperature = 270°K), each containing 1 mm of integrated liquid. The difference in the component spectra is due primarily to the strong dependence of liquid water absorption on temperature. Over the 28°K decrease in cloud temperature, the absorption increases by a factor of ~2.

The detectability of significant changes in the atmosphere and sea surface properties from satellite microwave measurements is determined by the frequency-dependent sensitivities of brightness temperatures to the desired parameters. To illustrate the sensitivity spectra, satellite brightness temperatures have been calculated for models which depart from the nominal by changes in individual parameters which represent ~10–20% of their total expected variation. The resulting brightness temperature perturbation spectra are shown in Fig. 4, with ΔT_b representing the change from our nominal atmospheric and sea surface model.

The least important parameter considered is the surface atmospheric pressure. A 3 mb increase, which changes the oxygen and vapor absorption slightly, is not significant for 5–40 GHz measurements. Variability over the full range of open ocean surface pressures will have a negligible effect on satellite measurements.

An increase in the tropospheric temperature by 3°K will increase the atmosphere's effective emitting temperature by ~1% at all frequencies and decrease the opacity by varying amounts due to the inverse dependence of both vapor and oxygen absorption on temperature. The net effect is an increase of the satellite T_b by ~0.7°K at the vapor absorption line center and a decrease of ~0.2–0.3°K at the higher frequencies where the opacity drop exceeds 1%.

An increase of 5°K from the assumed nominal model T_s of 295°K produces satellite T_b perturbations of ~2°K at the lower frequencies, zero at ~32 GHz and small decreases at the higher frequencies. For 5°K T_s variations relative to a different initial value, the shape of the perturbation spectrum is maintained but shifted in frequency. For example, a 5°K T_s variation about a value of 282°K produces a null effect at ~20 GHz.

For a wind speed increase of 3 m/s (above the threshold value of 7 m/s), the emissivity versus wind speed model produces ~3°K increase in satellite brightness temperatures from 10–40 GHz, consistent with the aircraft experimental data [53], [54]. The decrease in the effect below 10 GHz is due to the decrease in effective foam coverage for the Wilheit wind speed model [57]. The slight depression in the effect near 22 GHz is due to the reduction of the reflected atmospheric component at the highest opacities.

The effect of water vapor is clearly dominant in the 20–25 GHz region. The sensitivity at the 22.2 GHz vapor line center varies significantly with the height distribution of the vapor. This is much less true at the primary TMR vapor sensing channel at 21 GHz as described below. Above 30 GHz cloud liquid has the strongest signature and the TMR 37 GHz channel's primary function is to correct for this effect. It is noteworthy that the perturbation spectrum due to liquid has a local minimum near 22 GHz due to attenuation of the cloud emission by water vapor. This results in cloud liquid effects on satellite brightness temperatures which are very nearly equal at the TMR 18 and 21 GHz frequencies. We

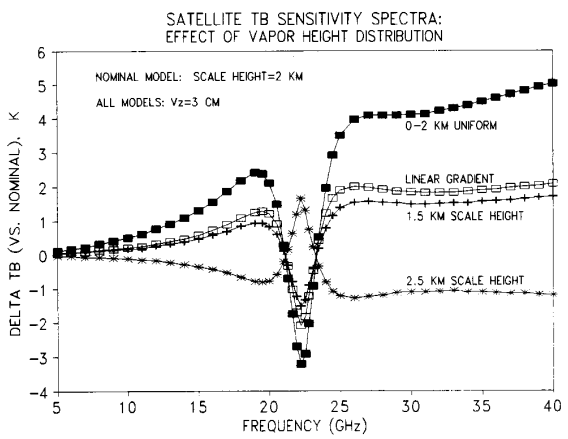

Fig. 5. Sensitivity spectra of satellite brightness temperatures from 5–40 GHz due to variability in the height distribution of water vapor. The integrated vapor content is 3.0 cm for all cases.

would thus expect that the atmospheric vapor burden and path delay will be very strongly correlated with the 21–18 brightness temperature difference, with other factors, such as variations in tropospheric and sea surface temperature and in wind speed, adding only small perturbations to the 21–18 difference.

An important additional effect is due to the pressure broadening of the 22.2 GHz vapor absorption feature. For a fixed vapor burden, the absorption and resultant T_b spectra depend on the height distribution of the vapor. The sensitivity is illustrated in Fig. 5 which shows the T_b perturbations produced by redistributing the V_z =3.0 vapor burden. The cases of scale heights = 1.5, 2.5 are realistic deviations from the nominal vapor scale height of 2.0 km. The linear gradient and uniform 2 km layer cases illustrate more extreme examples of the effect of concentrating the vapor at lower altitudes. As more of the vapor is concentrated near the surface, the absorption spectrum is broadened, with reduced emission at the line center and higher emission in the wings. The opposite effect is produced when more of the vapor resides at higher altitudes, increasing the atmospheric T_b near line center and reducing it in the wings. Note that at ~21.0 and 23.8 GHz the effect is very nearly zero, thereby strengthening the correlation between T_b measurements at these frequencies and the vapor burden. The occurrence of these null points ~1 line width from the absorption peak was the motivating factor for including these frequencies as the primary vapor sensing channels for the TOPEX and ERS-1 radiometers respectively. It should, however, be noted that operation at ~21.0 or 23.8 GHz, rather than at line center, makes the path delay error more sensitive to instrument calibration accuracy and measurement noise, due to the reduced absolute sensitivity to water vapor.

The sensitivities of the 3 TMR channels to all the significant atmospheric and sea surface variables are presented in Table I. The table also shows the full range of expected values of the variables for which TMR range corrections to the TOPEX altimeter data will be valid.

TABLE I
TMR BRIGHTNESS TEMPERATURE VARIATIONS OVER FULL RANGES OF ATMOSPHERIC AND SEA SURFACE PROPERTIES

Property	Full Range	Resultant Variation in TMR T_bs		
		18 GHz	21 GHz	37 GHz
Integrated Vapor	0.3-7.0 cm	32 K	80 K	44 K
Cloud Liquid	0-1.5 mm	30	30	70
Effective Temp. of Troposphere	270-290 K	0.2	5.7	3.8
Sea Surface Temp.	273-300 K	2.3	3.1	9.9
Wind Speed, 20 m Above Surface	0-28 m/s	22.1	17.8	20.0

III. TMR Wet Path Delay Retrieval Algorithm

Two general approaches have been commonly employed for the interpretation of satellite microwave radiometer measurements in terms of atmospheric and sea surface properties. Estimation methods [14], [58], [59] seek an inverse solution to (5)–(9) by iteratively finding a set of atmospheric and sea surface properties which reproduce the measurements to a specified accuracy, usually reflective of the measurement errors. Statistical methods [1], [60] utilize retrieval coefficients based on correlations between atmospheric properties and modeled brightness temperatures, including the effects of measurement errors. The performance of both techniques depends primarily on modeling accuracy over the full range of encountered climate conditions. In practice, most production mode post-launch algorithms have relied on empirical fits of the brightness temperatures to ground truth measurements of the parameters in question [16], [18].

For the prelaunch TMR wet path delay algorithm, we have developed a two-step version of the statistical retrieval method intended to be globally applicable and to account for wind speed effects on the sea surface emissivity and the nonlinearities in the vapor contribution to satellite brightness temperatures. The data base archive includes both radiosonde and sea surface temperature and wind speed data with global representation. The algorithm utilizes retrieval coefficients which have been stratified in both wind speed and path delay range. The drawbacks normally associated with statistical retrievals, large errors when anomalous conditions are encountered, are limited by the following considerations. The sole mission-specified function of the TMR is to provide wet path delay corrections for the TOPEX/Poseidon altimeter range measurements. The anomalous conditions for which the statistical path delay algorithm performance would deteriorate-rain and high winds-will cause much larger errors in the altimeter range measurements. It is expected that for all conditions for which the altimeter data is valid, the modeled TMR path delay retrieval errors will be representative of the true algorithm precision.

A. Statistical Data Base

The TMR retrieval algorithm utilizes two sets of global data bases. The first consists of four years of radiosonde data (1979–1982) from 23 island radiosonde sites provided by the

TABLE II
TMR PATH DELAY ALGORITHM RETRIEVAL COEFFICIENTS

Cloud Liquid Retrieval:

$$L_z = -1.875 - 0.022*TB18 - 0.003*TB21 + .032*TB37 \text{ (mm)}$$

Wind Speed Retrieval:

$$W = -75.0 + 1.795*TB18 - 0.561*TB21 - 0.433*TB37 \text{ (m/s)}$$

Path Delay Retrieval:

$$PD = B0 + B18*\ln(280-TB18) + B21*\ln(280-TB21) + B37*\ln(280-TB37) \text{ (cm)}$$

	B0 Coefficients				
Path delay range	W=0	W=7	W=14	W=21	W=28
0-60	92.005	91.388	84.598	77.601	70.886
0-10	69.954	69.622	66.592	62.835	58.821
10-20	38.579	37.483	29.333	22.270	16.219
20-30	49.871	48.590	38.428	29.113	20.727
> 30	72.157	71.298	64.403	57.500	50.768

	B18 Coefficients				
Path delay range	W=0	W=7	W=14	W=21	W=28
0-60	39.845	39.945	41.339	42.788	44.118
0-10	55.369	55.389	55.667	56.149	56.669
10-20	57.542	57.817	59.807	61.427	62.679
20-30	50.071	50.381	52.835	54.998	56.824
> 30	42.088	42.253	43.553	44.803	45.931

	B21 Coefficients				
Path delay range	W=0	W=7	W=14	W=21	W=28
0-60	-71.315	-71.261	-70.952	-70.619	-70.211
0-10	-84.016	-83.952	-83.458	-82.958	-82.408
10-20	-74.729	-74.717	-74.550	-74.251	-73.802
20-30	-68.704	-68.685	-68.502	-68.190	-67.726
> 30	-66.777	-66.722	-66.237	-65.650	-64.932

	B37 Coefficients				
Path delay range	W=0	W=7	W=14	W=21	W=28
0-60	13.791	13.738	13.210	12.662	12.118
0-10	15.136	15.102	14.804	14.444	14.052
10-20	9.976	9.897	9.290	8.733	8.220
20-30	9.491	9.404	8.712	8.053	7.432
> 30	11.327	11.264	10.743	10.201	9.644

National Center for Atmospheric Research. The radiosondes provided atmospheric profiles of temperature, pressure, and dew point depression (which was converted to vapor density) at a normal rate of twice per day (0 and 12 hours UT). To estimate liquid density from the radiosonde data, a cloud model was required (see below). All of the radiosondes were checked for unreliable or physically unrealistic data, including large pressure gaps, inadequate sampling, and superadiabatic lapse rates. All radiosondes which indicated over 1.5 mm of liquid water were rejected since this level of integrated liquid almost always indicates rain [61]. The final radiosonde data base archive included over 20 000 soundings from the 23 sites. The sampled climatologies included latitudes extending from 60° S to 57° N with site-average path delays ranging from 5 to 32 cm.

The second set of archive data consisted of monthly averaged sea surface temperature and wind speed statistics for the latitude, longitude locations of the 23 island radiosonde launch sites. These were obtained from the 1987 SSM/I data for wind speed and the infrared Advanced Very High Resolution Radiometer (AVHRR/2, flown on the NOAA-9 satellite platform) data for sea surface temperature (62). The wind speed averages, originally referenced to a 10 m height in the SSM/I monthly maps, have been converted to the 20 m reference height used in the emissivity versus wind speed model, assuming neutral stability [63]. The site statistics ranged from 0–30°C in sea surface temperature and 5.5–14.0 m/s in monthly-averaged wind speed.

Using first the radiosonde data base, opacities and upwelling and downwelling atmospheric brightness temperatures were computed at the TMR frequencies using the radiative transfer equations (6), (7), and (9), and the absorption models described in Section II. Also for each radiosonde, path delays (3) and cloud liquid burdens were computed and added to the atmospheric data archive. The cloud model used to compute liquid water density from the radiosonde data was as follows. For atmospheric layers for which the radiosondes indicated relative humidities >94%, cloud liquid was deemed to be present [64]. The cloud liquid density profile was then calculated by assuming that half the amount of water corresponding to the difference in absolute humidity between the cloud base and the cloud altitude in question was in the form of liquid. The 0.5 factor for computing liquid density is based on aircraft measurements of liquid density within stratus and cumulus clouds [44]. An additional constraint was applied that at all levels within a cloud the liquid density was ≤ 2.0 g/m^3, near saturation for nonraining conditions.

After the atmospheric data archive was established, six separate computational data archives of related TMR brightness temperatures were generated for different wind speed assumptions. The first used the site- and month-dependent wind speed averages, with Rayleigh distribution, to add surface flux and reflected contributions to the atmospheric components and produce a set of TMR brightness temperatures for each radiosonde. The second through sixth computed archives of TMR brightness temperatures were generated assuming constant wind speeds of 0, 7, 14, 21, and 28 m/s. All six TMR T_b archives were generated using the site- and month-dependent sea surface temperature averages with a random Gaussian variation of 2°K applied.

B. Retrieval Coefficient Generation

The generation of retrieval coefficients began with a multilinear regression of cloud liquid and wind speed against the TMR brightness temperatures contained in the first computational archive. Gaussian errors of 0.5°K were applied to the simulated TMR data. The resulting coefficients provided the algorithm with a globally applicable estimate of liquid burden and wind speed. The linearized liquid burden retrieval is very approximate and serves only to provide the estimate of the small liquid water contribution to wet path delay (4).

Next, sets of path delay retrieval coefficients were generated using each of the complete simulated TMR archives two through six. The path delays were actually correlated with a logarithmic function of the observables, $\ln(280-T_b)$, which has been shown to vary more linearly with vapor content than the brightness temperatures themselves [60]. The resulting coefficients provided interpolation points for determining global (first step) path delay retrieval coefficients as a function of the estimated wind speed. The final, stratified sets of path delay coefficients were generated for subsets of the constant wind speed archives two through six by dividing each archive into four path delay ranges: 0–10, 10–20, 20–30, and >30 cm. The path delay stratified coefficients are used in the second step of the retrieval algorithm, which is applied after the wind speed and initial path delay estimate have been computed from the global coefficients. The complete sets of path delay, liquid, and wind speed retrieval coefficients are listed in Table II.

C. Algorithm Processing

The complete algorithm operates as follows. First, the processed TMR brightness temperatures are evaluated for conditions indicative of rain or land contamination. These conditions are flagged using maximum allowable T_b criteria and no path delay retrievals are produced. For unflagged data, the first step is estimation of cloud liquid and wind speed using the global coefficients and the measured TMR brightness temperatures:

$$L_z = l_0 + \Sigma l_\nu T_b(\nu) \quad \nu = 18, 21, 37 \tag{12}$$

$$W = w_0 + \Sigma w_\nu T_b(\nu). \quad \nu = 18, 21, 37 \tag{13}$$

Next, the vapor-induced path delay is retrieved in two steps. A first estimate is obtained using global (unstratified in path delay) coefficients determined from the wind speed estimate:

$$\mathrm{PD}^{(g)} = B_0^{(g)} + \sum B_\nu^{(g)} \ln[280 - T_b(\nu)] \quad n = 18, 21, 37. \tag{14}$$

The coefficients $B_0^{(g)}$, $B_\nu^{(g)}$, are determined by linear interpolation with respect to wind speed in the "0–60" rows of the path delay coefficients versus wind speed section of Table II.

Next, path delay values are computed using stratified coefficients for data base ranges with center points which bracket the initial path delay estimate:

$$\mathrm{PD}^{(1)} = B_0^{(1)} + \Sigma B_\nu^{(1)} \ln[280 - T_b(\nu)] \quad \nu = 18, 21, 37 \tag{15}$$

$$\mathrm{PD}^{(2)} = B_0^{(2)} + \Sigma B_\nu^{(2)} \ln[280 - T_b(\nu)] \quad \nu = 18, 21, 37 \tag{16}$$

where the linear coefficients $B_0^{(1)}$, $B_\nu^{(1)}$, $B_0^{(2)}$, $B_\nu^{(2)}$ are obtained by interpolation in wind speed in the appropriate path delay range rows of the path delay coefficients versus wind speed section of Table II. For example, if the initial path delay estimate, $\mathrm{PD}^{(g)}$, equals 12.3, then $\mathrm{PD}^{(1)}$ and $\mathrm{PD}^{(2)}$ will be computed using stratified coefficients based on path delay ranges of 0–10 and 10–20, respectively. If the initial path delay estimate is less than 5 or greater than 35, then only the lowest (0–10) or highest (>30) stratified coefficients are used in the second step.

The final vapor-induced path delay retrieval is obtained by an average of $\mathrm{PD}^{(1)}$ and $\mathrm{PD}^{(2)}$, weighted according to the proximity of the stratified path delay ranges' center points to the initial path delay estimate:

$$\mathrm{PD}^{(f)} = [0.5 + (\mathrm{PD}_b - \mathrm{PD}^{(g)})/10]\mathrm{PD}^{(1)} + [0.5 - (\mathrm{PD}_b - \mathrm{PD}^{(g)})/10]\mathrm{PD}^{(2)} \tag{17}$$

where PD_b = the common boundary of the two stratified path delay retrievals. This weighting insures that there will be no retrieval discontinuities across stratification boundaries. The final total wet path delay is found by adding the small liquid component to the vapor-induced component:

$$\mathrm{PD}_w = \mathrm{PD}^{(f)} + 1.6 L_z \tag{18}$$

where L_z is the retrieved liquid burden in mm, given by (12).

D. Algorithm Testing

The path delay retrieval algorithm (12)–(18) was tested to assess the uniformity of the residuals with climatology (site), cloud abundance, and wind speed. The procedure was to assign new values for sea surface temperature and wind speed, using the site and month-dependent statistics, and compute new TMR brightness temperatures for each radiosonde-derived atmosphere. The retrieval algorithm was then applied and residuals grouped according to site, liquid abundance, and assigned wind speed. The results are presented in Table III.

Note first, under the All Weather heading, the consistency in performance from site to site. With the exception of the Orcados site, for which the bias magnitude is 0.3 cm, the retrieval biases are all below the 0.2 cm level. The inherent retrieval performance, as indicated by the rms residuals, is also remarkably consistent, with All Weather values in the 0.21–0.46 cm range. This result is primarily due to the stratification of retrieval coefficients according to path delay range. When only the global (initial estimate) retrieval coefficients are used, the overall rms residuals are ~60% higher and the retrieval biases are larger and more site-dependent.

The effects of clouds, shown in the next four columns, indicate a slight decrease in performance with liquid abundance, due primarily to the sensitivity of the 37 GHz brightness temperature to cloud height. However, the all-site performance, shown in the last two rows of Table III, indicates that the 37 GHz channel satisfactorily accounts for the nonraining cloud effects.

Similarly, wind speed effects appear to be negligible when the path delay retrieval coefficients are stratified according to wind speed. As indicated in the last five columns of Table III, performance does not significantly vary over the 0–28 m/s wind speed range. Any actual variation in post-launch algorithm performance with wind speed will be indicative of errors in our assumed model of emissivity dependence on wind speed (Section IV-B, below).

The All Weather test residual (0.37 cm) and consistency of performance over a complete range of climatologies insures that the algorithm error will be a minor component of the overall path delay retrieval error budget (Section IV). In comparison, the pre-launch algorithm for SMMR path delay processing [60] predicted retrieval errors of 0.9 cm, and required considerable post-launch "tuning" to eliminate biases. The pre-launch SSM/I algorithm [65] attempted to minimize regional biases by stratifying retrieval coefficients into latitudinal and seasonal zones. This resulted in retrieval discontinuities at zone boundaries and led to the development of a nonlinear global algorithm based on radiosonde comparisons with the early SSM/I data [16]. This algorithm eliminated biases from the verification data set by regressing the SSM/I brightness temperatures against radiosonde measurements of integrated vapor, including a quadratic term for the 22.2 GHz channel. The inclusion of the quadratic term makes the algorithm more sensitive to anomalous conditions, especially heavy cloud cover, and screening procedures are required for identifying such conditions. In addition, the post-launch strategy of empirically regressing brightness temperature measurements

TABLE III
TMR PATH DELAY ALGORITHM RETRIEVAL PERFORMANCE VERSUS SITE, CLOUD LIQUID ABUNDANCE, AND WIND SPEED

ISL. SITE (PDmean/ Std. Dev.)	LAT. DDMM	LONG(E) DDDMM		ALL WEATHER	CLEAR	CLOUD LIQ. RANGE (mm) .001-.5	0.5-1.0	1.0-1.5	WIND SPEED RANGE m/s < 12	12-16	16-20	20-24	24-28
Orcadas (5.07/ 2.56)	-6045	31517	# RAOBS	100	22	68	8	2	61	21	8	7	3
			PD BIAS	0.30	0.32	0.24	0.31	0.76	0.23	0.36	0.49	0.38	0.48
			PD RMS	0.43	0.40	0.34	0.38	0.83	0.41	0.44	0.55	0.40	0.49
Campbell (7.27/ 2.30)	-5233	16909		700	125	436	84	50	422	156	71	38	14
				0.04	0.03	0.02	0.03	0.13	0.00	0.08	0.08	0.15	0.11
				0.18	0.18	0.17	0.17	0.21	0.18	0.16	0.17	0.24	0.22
Marion (7.60/ 8.99)	-4653	3752		833	584	259	5	3	425	174	126	54	54
				0.17	0.23	0.04	0.10	-0.10	0.11	0.23	0.25	0.28	0.23
				0.29	0.30	0.26	0.26	0.35	0.26	0.30	0.33	0.36	0.29
Chatham (9.64/ 3.28)	-4357	28326		675	304	304	44	27	471	124	55	19	6
				0.02	0.06	-0.02	-0.06	0.07	0.00	0.03	0.05	0.11	0.07
				0.31	0.24	0.37	0.19	0.34	0.34	0.20	0.18	0.26	0.24
Raoul (14.68/ 4.98)	-2915	18205		334	184	133	17	5	275	42	14	3	0
				0.05	0.07	0.00	0.07	0.33	0.05	0.07	0.03	0.10	—
				0.33	0.31	0.29	0.33	0.72	0.33	0.34	0.16	0.18	—
Easter (15.79/ 4.25)	-2709	25035		204	88	98	9	10	178	19	7	0	0
				0.06	0.11	0.01	-0.07	0.17	0.05	0.10	0.08	—	—
				0.29	0.33	0.24	0.27	0.22	0.29	0.28	0.29	—	—
Trinidad (17.40/ 4.31)	-2003	33041		387	351	36	2	2	339	42	6	0	0
				0.14	0.16	-0.06	-0.22	0.08	0.13	0.25	0.04	—	—
				0.37	0.38	0.29	0.26	0.08	0.37	0.39	0.43	—	—
Pago (30.23/ 5.78)	-1420	18917		270	80	127	39	19	248	19	3	0	0
				0.07	0.12	0.04	0.11	0.01	0.07	0.05	0.08	—	—
				0.32	0.34	0.26	0.40	0.38	0.32	0.25	0.48	—	—
Majuro (31.76/ 5.93)	0705	17123		433	197	183	32	19	366	44	15	8	1
				0.18	0.29	0.11	0.15	-0.08	0.16	0.28	0.40	0.09	0.28
				0.46	0.48	0.44	0.47	0.39	0.45	0.44	0.73	0.34	0.28
Koror (31.98/ 5.52)	0720	13429		541	204	263	28	29	474	52	11	3	1
				0.16	0.27	0.12	0.11	0.05	0.14	0.28	0.33	0.05	0.62
				0.43	0.48	0.36	0.33	0.38	0.42	0.49	0.40	0.12	0.62
Kwajalein (32.18/ 5.65)	0844	16744		728	287	337	57	38	582	104	33	11	2
				0.01	0.13	-0.02	-0.07	-0.20	-0.02	0.12	0.21	0.23	0.11
				0.37	0.32	0.29	0.31	0.52	0.37	0.39	0.35	0.34	0.18
Yap (31.41/ 6.16)	0929	13805		626	206	295	63	51	556	51	15	5	0
				0.11	0.21	0.09	0.08	0.02	0.10	0.13	0.41	0.22	—
				0.35	0.38	0.32	0.37	0.32	0.35	0.30	0.49	0.24	—
SanAndres (29.36/ 6.23)	1235	27817		283	133	121	18	8	244	26	13	0	0
				-0.11	0.03	-0.22	-0.17	-0.18	-0.12	-0.02	-0.07	—	—
				0.41	0.38	0.35	0.49	0.25	0.45	0.50	0.43	—	—
Kingston (26.25/ 5.69)	1756	28313		1316	736	471	81	40	1197	107	13	0	0
				0.18	0.26	0.08	0.05	0.09	0.17	0.24	0.24	—	—
				0.41	0.44	0.35	0.32	0.38	0.40	0.42	0.42	—	—
Hilo (20.18/ 4.05)	1943	20456		1709	636	766	166	98	1389	226	81	13	2
				-0.01	0.08	-0.11	-0.05	0.11	-0.02	0.02	-0.03	0.05	-0.28
				0.30	0.34	0.27	0.24	0.28	0.30	0.30	0.26	0.37	0.36
Ishigaki (26.68/ 8.58)	2420	12410		1763	882	608	147	79	1345	279	105	29	7
				0.05	0.15	-0.05	-0.08	-0.05	0.04	0.07	0.08	-0.04	-0.16
				0.43	0.45	0.41	0.42	0.35	0.44	0.40	0.41	0.46	0.34
Minamid. (25.05/ 8.81)	2550	13114		1821	958	649	115	68	1448	259	94	20	1
				0.07	0.16	-0.02	-0.08	0.02	0.05	0.16	0.11	0.03	-0.09
				0.39	0.40	0.36	0.34	0.46	0.39	0.38	0.42	0.27	0.09
Chichij. (24.26/ 8.50)	2705	14211		1845	1167	538	82	44	1359	308	139	32	7
				0.03	0.10	-0.04	-0.21	-0.08	0.02	0.08	0.08	0.06	0.16
				0.45	0.37	0.34	1.34	0.34	0.48	0.33	0.37	0.43	0.34
Midway (17.95/ 5.95)	2813	18238		887	466	330	63	29	700	132	46	9	1
				0.06	0.08	0.03	0.03	0.11	0.05	0.09	0.10	0.14	0.23
				0.33	0.34	0.31	0.34	0.31	0.33	0.35	0.31	0.27	0.23
Bermuda (17.86/ 7.55)	3222	29519		797	472	277	35	16	612	132	33	16	5
				-0.01	-0.01	-0.01	0.00	0.09	-0.02	0.03	0.02	0.09	-0.13
				0.36	0.36	0.33	0.32	0.55	0.36	0.34	0.31	0.32	0.41
Adak (7.85/ 4.59)	5153	18321		943	235	498	120	58	651	156	96	29	14
				0.15	0.08	0.11	0.21	0.27	0.11	0.24	0.25	0.21	0.36
				0.37	0.25	0.28	0.41	0.48	0.37	0.36	0.41	0.27	0.55
St. Paul (6.94/ 3.68)	5709	18947		1732	398	1056	154	92	1214	280	144	65	30
				0.08	0.08	0.04	0.10	0.28	0.04	0.16	0.21	0.20	0.32
				0.30	0.21	0.23	0.34	0.51	0.28	0.29	0.37	0.28	0.47
Kodiak (7.99/ 4.39)	5745	20730		1670	648	723	172	91	1266	251	118	31	5
				0.06	0.11	-0.04	0.10	0.25	0.03	0.17	0.16	0.24	0.37
				0.31	0.27	0.26	0.34	0.47	0.31	0.30	0.28	0.34	0.46
All (19.09/ 10.87)	—	—		20597	9363	8576	1541	878	15822	3004	1246	392	153
				0.07	0.13	0.00	0.02	0.09	0.05	0.13	0.14	0.16	0.21
				0.37	0.36	0.34	0.45	0.44	0.38	0.34	0.35	0.33	0.37

against ground truth does not address instrument calibration errors. For TMR it is anticipated that the stratified two-step algorithm performance will be sufficient to separate instrument calibration and retrieval modeling errors in the post-launch verification analysis.

In the final stages of our algorithm development, we computed two-frequency retrieval coefficients in the event that either the 18 or 37 GHz TMR channels fail. (The primary vapor sensing channel at 21 GHz has a backup.) The algorithms were identical to the three-frequency case in structure, including

stratification in both wind speed and path delay range. The two-frequency algorithms were tested on the same simulated TMR brightness temperature data base. The results, shown as all-site retrieval biases and rms residuals versus cloud liquid and wind speed conditions in Table IV, demonstrate the limitations of two-frequency path delay algorithms. These comparisons should be carefully considered in assessing cost versus performance issues relevant to the choice of two- or three-frequency radiometers to support future altimeter missions.

Although the overall two-frequency performance, as measured by the All Weather rms residuals, appears to be acceptable for a range correction error budget of 1.5 cm, significant biases will occur for anomalous conditions. When only the 18 and 21 GHz channels are included, the detectability of heavy cloud conditions is lost, and retrieval biases of 1.5–2.0 cm can be expected when such regions are encountered. When only the 21 and 37 GHz channels are included, the capacity for radiometer detection of wind speed is lost and clearly unacceptable biases (2–5 cm) are predicted for wind speeds above 16 m/s (~9% of the expected conditions). Because the accompanying altimeter measurements provide an independent measurement of wind speed, the 21, 37 GHz two-frequency performance could potentially approach the three-frequency accuracy by including the altimeter wind speed estimates in the path delay algorithm processing. Real time independent estimates of cloud cover would not be available and maximum performance for an 18, 21 two-frequency system would require extensive post-processing effort.

These results demonstrate the drawback of assessing algorithm performance by only considering the all-weather residuals which are largely determined by the uniformity of the test conditions. The larger retrieval errors that occur for anomalous conditions which comprise less than 10% of the test data do not significantly affect the overall performance as measured by the all-weather residuals. They can, however, constitute an important source of altimeter bias in ocean regions which are commonly subject to heavy cloud or high wind conditions. When the anomalous cases are important, a better measure of algorithm performance is the maintenance of low biases and uniform residuals over the full range of encountered conditions of interest.

TABLE IV
COMPARISON OF TWO AND THREE FREQUENCY ALGORITHM PERFORMANCE

Bias, rms residual values in cm of path delay.

TEST DATA	# RAOBS	18,21,37 BIAS	18,21,37 RMS	18, 21 BIAS	18, 21 RMS	21,37 BIAS	21,37 RMS
All Weather	20597	0.07	0.37	0.01	0.80	0.31	1.41
Clear Only	9363	0.13	0.36	-0.24	0.54	0.58	1.38
Lz=.01-0.5 mm	8576	0.00	0.34	-0.18	0.56	0.24	1.35
Lz=0.5-1.0 mm	1541	0.02	0.45	0.73	0.99	-0.34	1.42
Lz=1.0-1.5 mm	878	0.09	0.44	1.61	1.75	-0.34	1.60
W < 12 m/s	15822	0.05	0.38	0.15	0.76	-0.23	0.91
W=12-16 m/s	3004	0.13	0.34	-0.30	0.80	1.49	1.69
W=16-20 m/s	1246	0.14	0.35	-0.57	0.95	2.63	2.75
W=20-24 m/s	392	0.16	0.33	-0.89	1.10	3.75	3.81
W=24-28 m/s	153	0.21	0.37	-1.33	1.49	5.15	5.22

IV. POST-LAUNCH VERIFICATION PLAN AND PATH DELAY ERROR ANALYSIS

A. In-Flight Verification

The six months following TOPEX/Poseidon launch have been dedicated to an in-flight verification/calibration effort for both altimeters and the TMR. For validation of the TMR performance, overflight comparisons will be made with data from both ground-based water vapor radiometers (WVR's) and selected island radiosondes. For the entire six month verification phase, three-channel WVR's, operating at 20.7, 22.2, and 31.4 GHz, have been deployed at the two primary mission verification sites: Lampedusa island in the Mediterranean for the Poseidon altimeter and the Harvest oil platform off the California coast for the NASA TOPEX altimeter. For one month each, a two-channel (20.7 and 31.4 GHz) WVR obtained overpass measurements at the island weather stations of Chichijima, south of Japan, and Norfolk, east of Australia. The latter two sites were chosen to obtain ground comparisons with the TMR data for conditions at the high and low ends of expected vapor conditions, respectively. Twenty-six island radiosonde sites were chosen based on the criterion of proximity to the TOPEX groundtrack (<50 km).

TMR comparisons with both ground-based WVR's and radiosondes are complimentary in the following sense. The WVR's provide direct measurements of the downwelling atmospheric flux and opacity, independent of any assumptions regarding atmospheric absorption properties. Because the upwelling and downwelling flux components are equal to within a few tenths of a Kelvin, the WVR measurements provide a direct calibration of TMR brightness temperatures to within the accuracy of the sea surface flux model. The comparisons depend strongly on the uniformity of conditions between the TMR and WVR fields of view so that cloud-free conditions are required. The conversions of the WVR channel measured fluxes to the TMR frequencies introduces negligible error because the vapor absorption model line shape is well constrained [37], [67]. The best comparisons are obtained for calm sea conditions when the surface flux contribution to the TMR $T_b s$ can be predicted with ~2°K accuracy. (Sea surface temperature and wind speed measurements are also obtained at the verification sites.) By averaging a sufficient number of the high quality WVR comparisons for a range of atmospheric vapor conditions, absolute calibration of the TMR brightness temperature measurements can be attained to the 2°K uncertainty level of the sea surface specular flux model. In terms of relative calibration, channel-to-channel offset accuracies to the 0.5°K level should be attainable. Because of the strong correlation of path delay with the 21–18 T_b difference, remaining errors due to the calm sea flux model uncertainty have negligible effect on the TMR path delay retrieval performance.

While the WVR's are primarily useful for TMR instrument calibration, the radiosonde comparisons provide a direct test of the path delay retrieval algorithm. In particular, plausible errors in our assumed model for vapor absorption, which constitute the largest source of uncertainty in the retrieval algorithm, will be tested by the radiosonde measurements of path delay which are not dependent on absorption model assumptions. Due to the significant spatial and temporal decor-

relations between the TMR and radiosonde measurements, a large volume of radiosonde comparisons will be required for in-flight fine-tuning of the TMR retrieval algorithm. The results of the TMR verification phase effort will be published in [66].

B. Retrieval Algorithm Error Budget

The all-site, all-weather rms residual value (0.37 cm) indicated in the bottom line of Table III represents the inherent retrieval error produced by an algorithm with zero modeling errors and perfect TMR T_b measurements of atmospheric and sea surface conditions which are representative of the range of conditions included in the algorithm's statistical data base. The inherent error includes the effects of variations in atmospheric and sea surface conditions largely uncorrelated with path delay, cloud liquid or wind speed which cause TMR T_b perturbations. For example, the variability in the height distribution of water vapor contributes to the inherent error. By using a two-step path delay retrieval algorithm, stratified both in wind speed and path delay range, this inherent algorithm uncertainty can be reduced to the 0.4 cm level. This, however, is not the dominant algorithm error.

Errors in our assumed models of atmospheric absorption and sea surface flux can produce both offset and scale errors in the application of the TMR path delay retrieval algorithm to real atmospheres. Because the path delay is strongly correlated with brightness temperature differences between the TMR channels, the frequency dependence of modeling errors is particularly important. In assessing the model induced uncertainties, we will begin with the vapor absorption model, known to be the dominant source of algorithm scale errors for vapor related retrievals. Other modeling uncertainties will then be analyzed to determine their relative significance for the path delay algorithm error budget.

The impact of vapor absorption model errors on the path delay retrieval accuracy is straightforward. If our assumed model is 5% high at all 3 TMR frequencies, then the retrieved path delays will be 5% low in the absence of other error sources. This translates into retrieval errors of ~1–2 cm in path delay for moderate to high vapor conditions. If the model error resides in the vapor absorption model line shape, then the retrieval error will depend on the relative model accuracies at the TMR frequencies. Based on both laboratory [67] and field [37] measurements, it is unlikely that line shape model inaccuracies are significant. Rather, the 22.2 GHz line strength constitutes the major source of modeling uncertainty. Calibration of the atmospheric vapor absorption near 22 GHz has relied almost entirely on comparisons of radiosonde measurements with WVR's. The accuracy and consistency of radiosonde humidity measurements has been a subject of considerable debate [68], [69]. Estimates in the 3–10% range for integrated vapor are most common. Special care must be taken to use only radiosonde data for which the humidity measurements are reliable. This often requires the elimination of data below the 20% relative humidity level and soundings which have passed through clouds. By applying these selection criteria to a recent set of radiosonde-WVR comparisons, we estimate the accuracy of the resultant vapor absorption model to be at the 4% level [37]. This translates to a 0.8 cm contribution to the path delay algorithm retrieval budget for average vapor conditions.

Modeling uncertainties for the oxygen and specular sea surface flux contributions to the TMR $T_b s$ will translate into small offset errors in the path delay retrievals. The effects can be assessed by considering a simplified global average version of the path delay retrieval algorithm. In terms of brightness temperature dependencies, the statistical data base yields the regression fit

$$\Delta \mathrm{PD} = \text{constant} - 0.48T_b(18) + 0.73T_b(21) - 0.08T_b(37) \tag{19}$$

$$\Rightarrow \Delta \mathrm{PD} = -0.48\delta T_b(18) + 0.73\Delta T_b(21) - 0.08\Delta T_b(37). \tag{20}$$

Equation (20) provides an estimate of the path delay uncertainties produced by frequency-correlated error sources. We expect that errors in the atmospheric absorption and sea surface emissivity models fall in this category; i.e., the frequency variation of the errors is constrained. For oxygen, which contributes ~7°K to $T_b(18)$ and $T_b(21)$, and ~17°K to $T_b(37)$ (see Fig. 3), the estimated uncertainty is 5%. If we assume this error is frequency independent, then the net PD biasing effect is

$$\Delta \mathrm{PD} = -.48(.05^*7) + .73(.05^*7) - .08^*(.05^*17) = .02 \text{ cm}.$$

Thus, a frequency-independent scale error in the oxygen absorption model has negligible effect on the PD retrievals. Even for a pathological case, in which the model error is +5% at 18 and 21 GHz and −5% at 37 GHz, the retrieved path delay bias is ~0.15 cm, negligible relative to the error due to the vapor absorption model uncertainty.

For the sea surface specular emissivity, a similar analysis reveals that the model uncertainties will yield path delay retrieval errors of ~0.1 cm. This assumes that the specular flux component uncertainty is 1°K at 18 and 37 GHz and 2°K at 37 GHz, as discussed in Section II. In the unlikely event that the modeling errors are pathological (of opposite sign at 37 versus 18, 21), the PD retrieval bias is 0.4 cm. In addition, the in-flight calibration using WVR's will partially correct offset errors of 1–2°K magnitude; i.e., discrepancies between the WVR predictions and actual measurements of TMR brightness temperatures at the 1–2°K level will be corrected by subtracting the indicated offsets from the TMR calibration. There will be no way of knowing whether the offsets are due to instrument calibration or modeling errors. However, in terms of the effect on algorithm performance, the corrections will reduce the PD biases to the 0.1–0.3 cm level, and it will not matter whether the errors are instrument or model related.

For liquid absorption, it is reasonable to assume that the absorption model fractional error is independent of frequency so that the effect scales with the brightness temperature component due to liquid. We consider an extreme case of a 5% absorption model error and a cloud with 1 mm of liquid at 4–4.5 km altitude. For such a case the nominal absorption model predicts liquid T_b contributions of 25°K at

18 and 21 GHz and 54°K at 37 GHz (Fig. 3). Again applying (20), the net PD retrieval error is 0.1 cm. This result again demonstrates the robustness of the three-frequency path delay retrieval. The path delay depends primarily on the interchannel brightness temperature differences, with the 18 and 37 GHz measurements primarily providing corrections for variable sea surface flux and cloud liquid. Thus, any modeling errors which are strongly correlated in frequency will be largely compensated in the path delay retrieval algorithm.

For the sea surface flux dependence on wind, two effects of modeling errors on the path delay algorithm must be considered. The first is that path delay retrieval coefficients vary with the algorithm estimate of wind speed. Thus, biases in the wind speed estimate will bias the path delay retrieval coefficient selection and subsequent PD retrieval. Analysis of the PD coefficient wind speed dependence (Table II) reveals an average path delay retrieval bias of ~0.1 cm for each 2 m/s error in the estimated wind speed. Using the wind speed retrieval coefficients and reasonable estimates for the uncertainties in the wind speed effect on TMR brightness temperatures, it can be shown that the bias uncertainty in the wind speed estimate is at the 2 m/s level, with resultant PD retrieval errors at the 0.1 cm level.

The second effect of wind speed modeling errors is on the measured brightness temperatures and can be assessed using (20). Our adopted wind speed model essentially produces 1°K of T_b increase in each TMR channel for each m/s of wind speed above the 7 m/s threshold. Based on the aircraft data [53], [54], a reasonable estimate of the uncertainty in the wind speed effect is 0.3 K/m/s. If this is the error at all three TMR frequencies, (20) reveals the resultant path delay retrieval bias to be ~0.04 cm for each m/s of wind speed above 7 m/s. For W =20 m/s conditions, the PD retrieval bias would be 0.55 cm, still smaller than the uncertainty due to the vapor absorption model, and probably inconsequential when the small fraction of W >20 m/s cases and the larger altimeter errors are considered.

For the wind speed modeling error we must also consider the possibility that the error is frequency dependent. Evidence exists [56] that the wind speed effect at 37 GHz may be up to ~50% higher than at the lower TMR frequencies. If this were the case, the resultant PD retrieval error would be due primarily to the 37 GHz coefficient in (20), but would remain less than 0.5 cm for wind speeds up to 20 m/s.

Based on the above analysis, our estimated retrieval algorithm error budget is shown in Table V for global and four subsets of atmospheric conditions. Both inherent and model induced algorithm errors are included. The terms "Cloudy" and "Windy" refer to conditions of 1 mm of nonprecipitating cloud liquid and a wind speed of 20 m/s respectively. Note that, for the full range of conditions for which the TMR range correction is valid, the retrieval algorithm errors lie in the range 0.9–1.1 cm. This is the estimated path delay retrieval accuracy for average vapor conditions and zero error brightness temperature measurements. To assess the total TMR-derived path delay accuracy, errors due to the antenna temperature calibration [29] and the conversion to altimeter footprint brightness temperatures [30] must also be considered.

TABLE V
TMR PATH DELAY RETRIEVAL ALGORITHM ERROR BUDGET

Error Source	Contribution to path delay algorithm error (cm)				
	All Weather	Clear, Calm	Calm, Cloudy	Clear, Windy	Cloudy, Windy
Inherent	0.37	0.36	0.44	0.36	0.46
Vapor abs. model	0.80	0.80	0.80	0.80	0.80
Oxy. abs. model	0.05	0.05	0.05	0.05	0.05
Liq. abs. model	0.03	0	0.10	0	0.10
Specular sea surface emis. model	0.20	0.20	0.20	0.20	0.20
Emissivity vs. wind speed model	0.21	0	0	0.55	0.55
RSS alg. error	0.93	0.90	0.94	1.06	1.10

C. Total TMR Path Delay Retrieval Error Budget

In addition to the retrieval algorithm errors, the overall wet troposphere range correction error budget must account for uncertainties in the TMR brightness temperature measurements and the conversion of path delay averaged over the TMR footprint to the smaller altimeter footprint. These errors will depend on the antenna temperature (calibration) accuracy, uncertainties related to the conversion of antenna temperatures to TMR main beam brightness temperatures, and the expected decorrelation between path delays averaged over the TMR and altimeter footprints.

Detailed analysis of the antenna temperature calibration, including stochastic noise, radiative transfer model residuals, and expected in-flight biases, yields accuracies in the range 0.5–0.6°K for all three TMR channels [29]. When these errors are included in the antenna pattern correction error budget, TMR main beam brightness temperature accuracies of 0.85, 0.79, and 0.88°K are obtained for the 18, 21, and 37 GHz channels [30]. If these errors are totally uncorrelated in frequency, then the resultant path delay uncertainty must be evaluated using the root sum square version of (20)

$$\Delta \mathrm{PD} = \{[(0.48)(0.85)]^2 + [(0.73)(0.79)]^2 + [(0.08)(0.88)]^2\}^{1/2}$$

$\approx$ 0.7 cm uncertainty due to T_b measurement errors. This value is conservative in the sense that part of the T_b errors will be frequency-correlated.

Additional errors will result due to the differing beam widths of the individual TMR channels and the assumed equivalence of the TMR-derived path delay and the path delay in the much smaller central footprints (~3 km) of the altimeters. Both effects have been evaluated using a statistical model of the expected spatial structure in water vapor [30].

For clear conditions, the analysis reveals that the differing TMR beam sizes produce an expected error of ~0.07 cm in path delay averaged over the largest TMR footprint. When clouds are present, the errors remain small (<0.2 cm in PD) except for scenes in which extensive cloud boundaries occur within ~25 km of the TMR beams' common axis. For such cases, PD errors of ~0.5 cm can occur. Based on the

TABLE VI
TOTAL ERROR BUDGET FOR TMR WET TROPOSPHERE RANGE CORRECTION

Error Source	Path Delay Error Contribution (cm)
Antenna Temperature Calibration and Beam Pattern Correction	0.69
Decorrelation Between TMR and Altimeter Main Beams	0.30
Beam Size Differences for 3 TMR Channels	0.11
Path Delay Retrieval Algorithm Error	0.93
RSS Total Error	1.20

expectation that the worst case cloud scenes occur less than 10% of the time, we estimate an average PD error component of 0.11 cm due to the unequal TMR beam sizes.

The error in equating the altimeter footprint path delay to the TMR-derived path delay is evaluated from calculations of the expected differences in path delay averaged over concentric areas of different sizes. Using experimentally determined parameters for the spatial structure of water vapor, and taking 3 and 40 km as representative of the altimeter and TMR footprints, we find the expected PD decorrelation error component to be 0.3 cm [30]. A summary of all contributions to the overall TMR range correction error budget is given in Table VI.

The total error is dominated by the retrieval algorithm error which, in turn, is dominated by the vapor absorption model uncertainty (Table V). In-flight calibration of the TMR path delay retrievals cannot be expected to improve the performance to levels significantly below 1.2 cm because the ground "truth" radiosonde errors are the limiting factor in vapor absorption model calibration. For the current level of absorption model uncertainty (~4%), the bottom line retrieval performance of 1.2 cm is consistent with the mission specifications for the wet troposphere contribution to the overall altimeter error budget [25].

ACKNOWLEDGMENT

This paper presents the results of one phase of research conducted at the Jet Propulsion Laboratory, California Institute of Technology, under contract with the National Aeronautics and Space Administration.

REFERENCES

[1] J. W. Waters, K. F. Kunzi, R. L. Pettyjohn, and D. H. Staelin, "Remote sensing of atmospheric temperature profiles with the Nimbus 5 microwave spectrometer," *J. Atmos. Sci.*, vol. 32, pp. 1953–1969, 1975.

[2] R. W. Spencer, J. Christy, and N. C. Grody, "Global atmosphere temperature monitoring with satellite microwave measurements: Methods and results 1979–1984," *J. Clim. Appl. Meteorol.*, vol. 3, pp. 1111–1128, 1990.

[3] R. W. Spencer and J. C. Christy, "Precise monitoring of global temperature trends from satellites," *Science*, vol. 247, pp. 1558–1562, 1990.

[4] T. J. Schmugge, J. M. Meneely, A. Rango, and R. Neff, "Satellite microwave observations of soil moisture variations," *Water Resources Bull.*, vol. 13, no. 2, 1977.

[5] R. K. Moore, F. T. Ulaby, and A. Sobti, "The influence of soil moisture on the microwave response from terrain as seen from orbit," in *Proc. 10th Int. Symp. Remote Sensing of Environment*, Ann Arbor, MI, 1975.

[6] P. Gloersen, T. T Wilheit, T. C. Chang, W. Nordberg, and W. J. Campbell, "Microwave maps of the polar ice of the earth," *Bull. Am. Meteor. Soc.*, vol. 55, no. 12, pp. 1422–1448, 1974.

[7] D. J. Cavalieri, P. Gloerson, and W. J. Campbell, "Determination of sea ice parameters with the Nimbus 7 SMMR," *J. Geophys. Res.*, vol. 89, pp. 5355–5369, 1984.

[8] M. R. Anderson, R. G. Crane, and R. G. Barry, "Characteristics of arctic ice determined from SMMR for 1979: Case studies in the seasonal sea ice zone," *Adv. Space Res.*, vol. 5, pp. 257–261, 1985.

[9] K. F. Kunzi, S. Patil, and H. Rott, "Snow-cover parameters retrieved from Nimbus-7 scanning multichannel microwave radiometer (SMMR) data," *Rev. Geophys. Space Phys.*, vol. 22, pp. 452–467, 1984.

[10] N. C. Grody, "Classification of snow cover and precipitation using the special sensor microwave imager," *J. Geophys. Res.*, vol. 96, pp. 7423–7435, 1991.

[11] T. T. Wilheit, A. T. C. Chang, M. S. V. Rao, E. B. Rodgers, and J. S. Theon, "A satellite technique for quantitatively mapping rainfall rates over the oceans," *J. Appl. Meteorol.*, vol. 16, pp. 551–560, 1977.

[12] J. A. Weinman and P. J. Guetter, "Determination of rainfall distributions from microwave radiation measured by the Nimbus-6 ESMR," *J. Appl. Meteorol.*, vol. 16, pp. 437–442, 1977.

[13] L. J. Allison, E. B. Rodgers, T. T. Wilheit, and R. W. Fett, "Tropical cyclone rainfall as measured by the Nimbus 5 electrically scanning microwave radiometer," *Bull. Am. Meteor. Soc.*, vol. 55, pp. 1074–1089, 1974.

[14] N. C. Grody, "Remote sensing of atmospheric water content from satellites using microwave radiometry," *IEEE Trans. Ant. Propogat.*, vol. AP-24, pp. 155–162, 1976.

[15] J. C. Alishouse, "Total precipitable water and rainfall determinations from Seasat scanning multichannel microwave radiometer," *J. Geophys. Res.*, vol. 83, pp.1929–1935, 1983.

[16] J. C. Alishouse, S. A. Snyder, J. Vongsathorn, and R. R. Ferraro, "Determination of oceanic total precipitable water from the SSM/I," *IEEE Trans. Geosci. Remote Sensing*, vol. 28, pp. 811–816, 1990.

[17] D. H. Staelin, K. F. Kunzi, R. L. Pettyjohn, R. K. L. Poon, R. W. Wilcox, and J. W. Waters, "Remote sensing of atmospheric water vapor and liquid water with the Nimbus-5 microwave spectrometer," *J. Appl. Meteorol.*, vol. 15, pp. 1204–1214, 1976.

[18] J. C. Alishouse, J. B. Snyder, E. R. Westwater, C. T. Swift, C. S. Ruf, S. A. Snyder, J. Vongsathorn, and R. R. Ferraro, "Determination of cloud liquid water content using SSM/I," *IEEE Trans. Geosci. Remote Sensing*, vol. 28, pp. 817–822, 1990.

[19] A. Blume, B. M. Kendall, and J. C. Fedors, "Measurements of ocean temperature and salinity via microwave radiometry," *J. Boundary-Layer Meteorol.*, vol. 13, p. 295, 1978.

[20] R. L. Bernstein and D. B. Chelton, "Large-scale sea surface temperature variability from satellite and shipboard measurements," *J. Geophys. Res.*, vol. 90, p. 11,619–11,630, 1985.

[21] F. W. Wentz, L. A. Mattox, and S. Peteherych, "New algorithms for microwave measurements of ocean winds: Applications to Seasat and the special sensor microwave imager," *J. Geophys. Res.*, vol. 91, pp. 2289–2307, 1986.

[22] P. C. Pandey, "Measurement of global oceanic winds from Seasat-SMMR and its comparison with Seasat-SASS and ALT derived winds," *IEEE Trans. Geosci. Remote Sensing*, vol. GE-25, pp. 670–676, 1987.

[23] M. A. Goodberlet, C. T. Swift, and J. C. Wilkerson, "Ocean surface wind speed measurements of the Special Sensor Microwave/Imager (SSM/I)," *IEEE Trans. Geosci. Remote Sensing*, vol. 28, pp. 823–828, 1990.

[24] N. C. Grody, "Remote sensing of the atmosphere from satellites using microwave radiometry," in *Atmospheric Remote Sensing By Microwave Radiometry*, M. A. Janssen, Ed. New York: Wiley, 1993, ch. 6.

[25] G. Carlisle, A. DiCicco, H. M. Harris, A. Salama, and M. Vincent, "TOPEX/Poseidon Project Mission Plan," Documentation no. D-6862, Rev. B, Jet Propulsion Laboratory, Pasadena, CA, 1991.

[26] E. G. Njoku, J. M. Stacey, and F. T Barath, "The Seasat Scanning Multichannel Microwave Radiometer (SMMR): Instrument description and performance," *IEEE J. Oceanic Eng.*, vol. OE-5, pp. 100–115, 1980.

[27] D. Jourdan, C. Boissier, A. Braun, and J .F. Minster, "Influence of wet tropospheric correction on mesoscale dynamic topography as derived from satellite altimetry," *J. Geophys. Res.*, vol. 95, pp. 17,993–18,004, 1990.

[28] ERS-DC Project Office, "Along track scanning radiometer and microwave sounder," Ref. DC-HO-PST-SY-008, Farnborough, Hants, UK, 1987.

[29] C. S. Ruf, S. J. Keihm, and M. A. Janssen, "TOPEX/Poseidon Microwave Radiometer (TMR): I. Instrument description and antenna temperature calibration," *IEEE Trans. Geosci. Remote Sensing,* vol. 33, pp. 125–137, 1995.

[30] M. A. Janssen, C. S. Ruf and S. J. Keihm, "TOPEX/Poseidon Microwave Radiometer (TMR): II. Antenna pattern correction and brightness temperature algorithm," *IEEE Trans. Geosci. Remote Sensing,* vol. 33, pp. 138–146, 1995.

[31] G. Elgered, "Tropospheric radio path delay from ground-based microwave radiometry," in *Atmospheric Remote Sensing by Microwave Radiometry,* M. A. Janssen, Ed. New York: Wiley, 1993, ch. 5.

[32] G. Boudouris, "On the index of refraction of air, the absorption and dispersion of centimeter waves by gasses," *J. Res. Natl. Bur. Stand., Sect. D,* vol. 67, pp. 631–684, 1963.

[33] R. J. Hill, R. S. Lawrence, and J. T. Priestly, "Theoretical and calculational aspects of the radio refractive index of water vapor," *Radio Sci.,* vol. 17, pp. 1251–1257, 1982.

[34] G. M. Resch, "Water vapor radiometers in geodetic applications," in *Geodetic Refraction,* F. K. Brunner, Ed. New York: Springer-Verlag, 1984.

[35] M. A. Janssen, "Introduction to the microwave remote sensing of atmospheres," in *Atmospheric Remote Sensing by Microwave Radiometry,* M. A. Janssen, Ed. New York: Wiley, 1993, ch. 1.

[36] H. J. Liebe, P. W. Rosenkranz, and G. A. Hufford, "Atmospheric 60-GHz oxygen spectrum: New laboratory measurements and line parameters," *J. Quant. Spectrosc. Radiat. Transfer,* vol. 48, pp. 629–643, 1992.

[37] S. J. Keihm, "Atmospheric absorption from 20–32 GHz: Radiometric constraints on the vapor and oxygen components," in *Proc. Specialist Meeting on Microwave Radiometry and Remote Sensing Applications,* Boulder, CO, 1992, pp. 211–218.

[38] E. R. Westwater, J. B. Snider, and M. J. Falls, "Ground-based radiometric observations of atmospheric emission and attenuation at 20.6, 31.65, and 90.0 GHz: A comparison of measurements and theory," *IEEE Trans. Ant. Propogat.,* vol. 38, pp. 1569–1580, 1990.

[39] L. Danese and R. B. Partridge, "Atmospheric emission models: Confrontation between observational data and predictions in the 2.5–300 GHz frequency range," *Astrophys. J.,* vol. 342, pp. 604–615, 1989.

[40] H. J. Liebe and D. H. Layton, "Millimeter-wave properties of the atmosphere: Laboratory studies and propogation modelling," Nat. Telecom. and Inform. Admin., NTIA Rep. 87–24, Boulder, CO, 1987.

[41] J. H. Van Vleck and V. S. Weisskopf, "On the shape of collision-broadened lines," *Rev. Mod. Phys.,* vol. 17, pp. 227–236, 1945.

[42] J. W. Waters, "Absorption and emission by atmospheric gasses," in *Methods of Experimental Physics.* New York: Academic Press, 1976, pp. 142–176.

[43] G. E. Becker and S. H. Autler, "Water vapor absorption of electromagnetic radiation in the centimeter wavelength range," *Phys. Rev.,* vol. 70, pp. 300–307, 1946.

[44] M. S. Malkevich, V. S. Kosolapov, and V. I. Statskiy, "Statistical characteristics of the vertical water content structure of cumulus clouds," *Izvestiya, Atmos. Ocean. Phys.,* vol. 17, 1981.

[45] W. H. Peake, "Interaction of electromagnetic waves with some natural surfaces," *IEEE Trans. Ant. Propogat. (Special Suppl.),* vol. AP-7, pp. S324–S329, 1959.

[46] T. T. Wilheit, "A model for the microwave emissivity of the ocean's surface as a function of wind speed," *IEEE Trans. Geosci. Electron.,* vol. GE-17, pp. 244–249, 1979.

[47] C. Cox and W. Munk, "Measurements of the roughness of the sea surface from photographs of the sun's glitter," *J. Opt. Soc. Am.,* vol. 44, pp. 838–850, 1954.

[48] A. Stogryn, "The apparent temperature of the sea at microwave frequencies," *IEEE Trans. Ant. Propogat.,* vol. AP-15, pp. 278–286, 1967.

[49] F. J. Wentz, "A two-scale scattering model for foam-free sea microwave brightness temperatures," *J. Geophys. Res.,* vol. 80, pp. 3441–3446, 1975.

[50] Y. A. Bespalova, V. M. Veselov, A. A. Glotov, Y. A. Militskii, V. G. Mirovskiy, *et al.*, "Sea-ripple anisotropy estimates from variations in polarized thermal emission of the sea," *Oceanology,* 1981.

[51] E. A. Bespalova, V. M. Veselov, V. E. Gershenzon, Y. A. Militskii, V. G. Mirovskii, *et al.*, "Surface wind velocity determination from measurements of the polarization anisotropy of microwave emission and backscatter," *Sov. J. Remote Sensing,* pp. 121–131, 1981.

[52] S. I. Gaydanskiy, V. Y. Gershenzon, and V. K. Gromov, "Detection of surface manifestations of internal waves in the ocean by microwave radiometry," *Izvestiya, Atmos. Oceanic Phys.,* vol. 24, pp. 731–735, 1988.

[53] W. Nordberg, J. Conaway, D. B. Ross, and T. Wilheit, "Measurements of microwave emission from a foam-covered wind driven sea," *J. Atmos. Sci.,* vol. 38, pp. 429–435, 1971.

[54] W. J. Webster, Jr., T. T. Wilheit, D. B. Ross, and P. Gloersen, "Spectral characteristics of the microwave emission from a wind-driven foam-covered sea," *J. Geophys. Res.,* vol. 81, pp. 3095–3099, 1976.

[55] L. A. Klein and C. T. Swift, "An improved model for the dielectric constant of sea water at microwave frequencies," *IEEE Trans. Ant. Propogat.,* vol. AP-25, pp. 104–111, 1976.

[56] F. J. Wentz, "Measurement of oceanic wind vector using satellite microwave radiometers," *IEEE Trans. Geosci. Remote Sensing,* vol. 30, pp. 960–972, 1992.

[57] T. T. Wilheit, "The effect of wind on the microwave emission from the ocean's surface at 37 GHz," *J. Geophys. Res.,* vol. 84, pp. 4921–4926, 1979.

[58] G. Bierman, F. Wentz, and R. Lipes, "Modern estimation techniques applied to microwave sensing of the marine boundary layer," in *Proc. Asilomar Conf. Circuits, Syst., Computers 12th,* 1978, pp. 101–106.

[59] F. J. Wentz, "A model function for ocean microwave brightness temperatures," *J. Geophys. Res.,* vol. 88, pp. 1892–1908, 1983.

[60] T. T. Wilheit and A. T. C. Chang, "An algorithm for retrieval of ocean surface and atmospheric parameters from the observations of the scanning multichannel microwave radiometer (SMMR)," *Rad. Sci.,* vol. 15, pp. 525–544, 1980.

[61] G. Elgered, B. Ronnang, E. Winberg, and J. Askne, "Satellite-Earth range measurements. I. Correction of the excess path length due to atmospheric water vapour by ground based radiometry," Res. Rep. 147, Onsala Space Observatory, Chalmers Univ. of Technology, 1985.

[62] D. Halpern, V. Zlotnicki, J. Newman, D. Dixon, O. Brown, and F. Wentz, "An atlas of monthly mean distributions of GEOSAT sea surface height, SSMI surface wind speed, AVHRR/2 sea surface temperature, and ECMWF surface wind components during 1987," Jet Propulsion Lab. Pub. 92-3, 1992.

[63] V. J. Cardone, "Specification of the wind distribution in the marine boundary layer for wave forecasting," Ph.D. dissertation, New York Univ., 1969.

[64] B. L. Gary, S. J. Keihm, and M. A. Janssen, "Optimum strategies and performance for the remote sensing of path-delay using ground-based microwave radiometers," *IEEE Trans. Geosci. Remote Sensing,* vol. GE-23, pp. 479–484, 1985.

[65] J. P. Hollinger, R. Lo, G. Poe, R. Savage, and J. Pierce, *Special Sensor Microwave/Imager Users Guide.* Washington, DC: Naval Res. Lab., 1987, p. 120.

[66] C. S. Ruf, S. J. Keihm, B. Subramanya, and M. A. Janssen, "TOPEX/Poseidon microwave radiometer performance and in-flight calibration," *JGR-Oceans TOPEX/Poseidon Special Issue,* in press.

[67] R. J. Hill, "Water vapor-absorption line shape comparison using the 22-GHz line: The Van Vleck–Weisskopf shape affirmed," *Radio Sci.,* vol. 21, pp. 447–451, 1986.

[68] W. P. Elliot and D. J. Gaffen, "On the utility of radiosonde humidity archives for climate studies," *Bull. Am. Meteor. Soc.,* vol. 72, pp. 1507–1520, 1991.

[69] B. E. Schwartz and C. A. Doswell, III, "North American rawinsonde observations: Problems, concerns, and a call to action," *Bull. Am. Meteor. Soc.,* vol. 72, pp. 1885–1896, 1991.

Stephen J. Keihm, for a photograph and a biography, see page 137 of this issue of this TRANSACTIONS.

Michael A. Janssen, for a photograph and a biography, see page 137 of this issue of this TRANSACTIONS.

Christopher S. Ruf (S'85–M'87–SM'92), for a photograph and a biography, see page 136 of this issue of this TRANSACTIONS.